Materials Research. 2025; 28: e20250296
DOI: https://doi.org/10.1590/1980-5373-MR-2025-0296

Investigation of Phase Formation, As-cast Microstructure, Microhardness and 3D Porosity in Quaternary Al – 5 wt.% Si – 4 wt.% Cu – 1 wt.% Ni Alloy Obtained Under Transient Heat-Flow Conditions

Matheus Carvalho Nascimento[a], Wysllan Jefferson Lima Garção[b], Paulo Felipe Júnior[c], Roberto Carlos Sales[a], Arthur Dias da Silva[a], Alexandre Furtado Ferreira[a,*]

[a]Universidade Federal Fluminense, Programa de Pós-Graduação em Engenharia Metalúrgica, 27255-125, Volta Redonda, RJ, Brasil.
[b]Instituto Federal do Rio de Janeiro, 27213-100, Volta Redonda, RJ, Brasil.
[c]Universidade do Estado do Rio de Janeiro, 27537-000, Resende, RJ, Brasil.

Received: February 05, 2025; Revised: May 12, 2025; Accepted: June 08, 2025

The present experimental investigation focuses on the phase formation, microstructural patterns, microhardness and 3D porosity for a quaternary Al – 5 wt.% Si – 4 wt.% Cu – 1 wt.% Ni alloy. Through the phase diagram and Thermo-Calc Scheil simulation, one can determine the growth sequence of the phases during the cooling process. With slow cooling curve and its first and second derivatives, one can find both liquidus and solidus temperatures. An approach based on the second derivative curve was adopted to determine the onset of solidification and subsequent phase transformations. These experimental results obtained with slow cooling curves are corroborated by those determined by Thermo-Calc software. An ingot of the quaternary aluminum alloy was produced by upward vertical unidirectional solidification under transient heat extraction conditions. Here, we used a water-cooled system to investigate the thermal parameters effects on the as-cast microstructure, microhardness and 3D porosity. The impacts of solidification thermal conditions on the microstructural patterns, microhardness and porosity formation were presented and discussed. Higher values of solidification thermal parameters and refined as-cast microstructures were key factors acting during solidification, which served to conditions changes in the Vickers microhardness and porosity formation along the casting. The relationship between porosity and cooling rate is presented and discussed from experimental equation, $P_C = -0.41\dot{T}^2+2.36\dot{T}+2.51$. This result indicates that porosity formation is closely connected to the said thermal parameter. With 3D image analysis, the distribution of porosity size in casting can be investigated. For positions close to the water-cooled system, porosity with smaller sizes, were predominant in casting. However, for positions away from the water-cooled system with lower cooling rates, porosity with higher sizes were observed.

Keywords: *Quaternary aluminum alloy, solidification parameters, thermal analysis, microhardness, 3D porosity.*

1. Introduction

Cast Al-Si-Cu alloys are widely considered in various engineering applications, especially in automotive industries, due to light weight, high strength and good castability. Vehicles built with aluminum parts are lighter and therefore consume less energy. These aluminum alloys have been used for automotive parts, for the transmission cases, converter housing and cylinder blocks. These parts, previously made of the cast iron, have been replaced by cast aluminum alloys, because of their contribution to an energy efficiency and lower levels of gas emission. Ternary Al-Si-Cu alloys are cast aluminum alloys widely considered because its excellent properties, such as high cast-ability, low density, low shrinkage rate and relatively high strength. On the other hand, cast aluminum alloys have not been always suitable for automotive industries. This is because cast defects are included in these cast components. Applications of cast aluminum alloys to the manufacture of critical safety parts, has been considerably restricted, Farina et al.[1]. In previous papers found in the literature, it was reported various kinds cast defects in these materials, e.g., cracks, abnormal microstructures and porosities. In continuous casting, molten metal is solidified into a cooled mould before subsequent rolling in the finishing mills. Under this condition, dendrite growth occurs from mould wall, resulting in contraction voids in the middle of the cast ingot. The mechanical properties, such as strength and elongation of these aluminum alloys decreases almost linearly with increase defect size. The reduction of the tensile properties is also affected by the type of cast defect. The reduction of the tensile properties is favored by the abnormal structure and contraction voids, which are included in the cast component, Li et al.[2].

*e-mail: alexandrefurtado@id.uff.br
Associate Editor: Hugo Sandim.
Editor-in-Chief: Luiz Antonio Pessan.

Solidification process is the main mechanism that occurs during casting. Understanding of thermal conditions, as well as structures, can lead to betters of the as-cast parts. Analysis of slow cooling curve, allows metallurgists and physicists to monitor the progress of phases transformation during solidification. Specifically, temperature-time curve provides an accurate assessment of the potential nucleation and modification states of the melt prior to casting. Thermal analysis has become very important to study of slow cooling curve due to it helps realize the desired properties in as-cast alloys. In addition, the derivative of the slow cooling curves allows the determination of the kinetics and dynamics of the thermal process that occur during the alloys crystallization[3-5].

On the other hand, research involving experiments of unidirectional solidification under a transient regime of heat extraction, has come attention in the last decade. The methodology allows investigation of the evolution of the solidified layers and its microstructure as a consequence of the solidification thermal conditions. Making it an attractive methodology to investigate these said conditions during the solidification of metals and their alloys. For upward directional solidification, the melt close to the solid/liquid interface, is rich in solute segregated from the solid region. This melt flows downward and the convection is confined in the interdendritic/intercellular regions, since the thermal gradient tends to stabilize density stratification in the melt. This phenomenon leads to cell/dendrite fragmentation to accommodate higher solute concentration in those regions[6-9].

The melt in the aluminum melt process may absorb hydrogen in the atmosphere and decompose the water that has accumulated on crucible furnace. If the melt absorbs excess hydrogen, it may affect the porosity of the final product. Metal degassing is an intermediate step in aluminum alloys production between the melting and casting. Due to the reaction with water vapor, hydrogen is mainly dissolved in liquid aluminum. In order to prevent the formation of holes during the casting, hydrogen is removed from liquid metal through degassed. Metal degassing is achieved by injecting an inert gas (argon), which is combined with hydrogen bubbles.

From this general framework that the present work is elaborated, highlighting the phase formation, microstructures, microhardness and porosity analysis in 3D images. The sequence of phase formation during the cooling process, it was calculated according to the Thermo-Calc Scheil simulation. The computer-aided cooling curve analysis (CA-CCA) with its first and second derivative, has been used to experimental validation of liquidus and solidus temperature. After the solidification experiment under slow cooling conditions, quaternary aluminum alloy ingot was obtained from upward vertical directional solidification under transient conditions of heat extraction. A water-cooled system has been adopted in order to investigate the effects of cooling rate and solidification speed on the microstructural growth, microhardness and 3D porosity along the casting. A microcomputed tomography was used in order to characterize the porosity formation with 3D images. Series of X-ray projection images was computed into cross-section images through the reconstruction computational process. Thus, these slices could be analyzed, further processed into 3D images. It stands out among results the thermal parameters effects on the tertiary dendritic arm spacings (λ_3), Vickers microhardness (H_V) and porosity. Higher cooling rates and refined microstructures were key factors acting during the solidification experiment, which served to conditions changes both in the microhardness and porosity. Through 3D images analysis, it can be investigated distribution of pores size along the casting. For positions near to the water-cooled system, one can observe that gas porosity with smaller sizes, were predominant in the casting. However, for positions away from the water-cooled system with lower cooling rates, porosity with higher sizes were observed.

2. Experimental Procedure

Firstly, phase diagram and equilibrium Scheil model revealing precipitation of phases during cooling of the quaternary aluminum alloy were calculated by Thermo-Calc software using the aluminum-based alloys databases - TCAL9, Ref[10].

An ingot of quaternary aluminum alloy (Al – 5 wt.% Si – 4 wt.% Cu – 1 wt.% Ni) was prepared in electrical resistance furnace at 700 °C. The materials were obtained from commercial purity metals, i.e. 99.9 wt.% aluminum, 99.8 wt.% silicon, 99.9 wt.% copper and 99.8 wt.% nickel. Its chemical composition was measured using a fluorescence X-ray spectrometry. During the melting, a steel rod with a 1 mm thick layer of insulating alumina was used to ensure homogeneity of the melt.

The experimental rig for slow cooling was developed by using a wooden chamber with a tick insulating blanket to achieve a very slow cooling rate. The molten aluminum alloy then was placed into this rig and allowed to solidify. The cooling rate was achieved by allowing the molten to cool naturally at room temperature. The temperature profile of the molten was determined by using one k-type thermocouple immersed about half into the molten metal height in the graphite crucible. The thermocouple was connected to a data-logger hardware which linked to a notebook, the data logger was set at 0.001 s intervals. The methodology adopted for slow cooling curve was previously described in greater detail in Refs[11,12]. For solidification experiment with slow cooling, its cooling rate was around 0.09 °C/s. The cooling curve was plotted, and the its first and second derivative were determined using a Tecplot Visualization and Analysis software (TECPLOT 360) to analyze the characteristic data. With cooling curve and its derivatives, the characteristic temperatures of liquidus (T_L) and solidus (T_S) were determined during cooling process.

After the solidification experiment under slow cooling, ingot of the quaternary alloy was melted in electrical resistance furnace at 700 °C. Subsequent to melting, the molten aluminum alloy was poured into a unidirectional solidification apparatus with water-cooling system, which favors high cooling rates at regions close to the bottom of mold. Figure 1 shows the details of the directional solidification casting assembly adopted for the present work. More details on the casting assembly can be found in Ref[9].

The solidification system was designed in such a way that the heat flux is extracted through the water-cooled bottom, promoting upward directional solidification. Adoption of such apparatus for the solidification experiment, allows natural

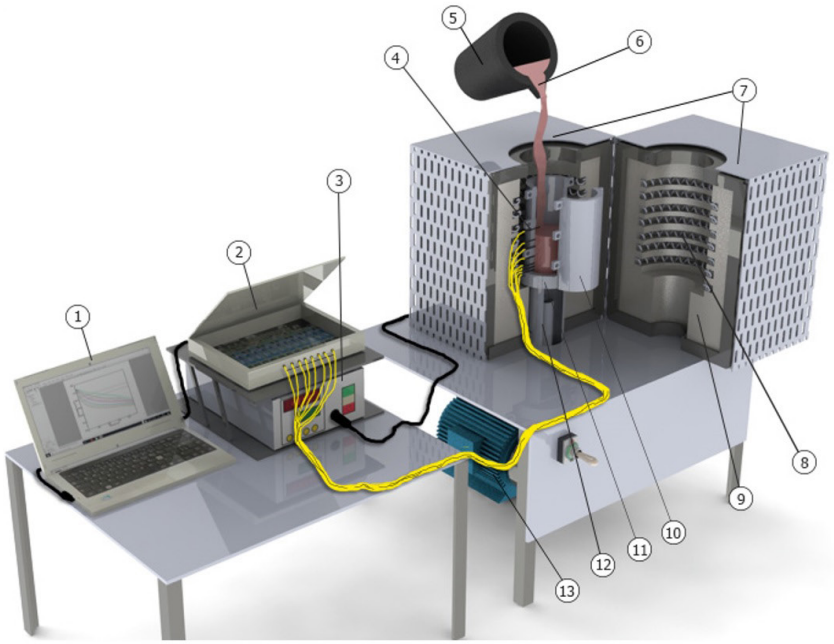

Figure 1. Representation of upward directional solidification apparatus.

convection to be minimized, as well as solute convection due to buoyancy forces if the rejected solute from the solid region has higher density than the material melt. The inner vertical surface was covered with a layer of insulating alumina to reduce the radial heat flux, and a cover made of a refractory material was used on the mold top, to minimize heat losses from the metal/air interface. A steel mold was used having an internal diameter of 50 mm and height of 140 mm. The mold bottom was closed with a steel chill with a thickness of 3 mm. The solidification apparatus has lateral electric heaters, so a desired superheat can achieve before the start of the experiment per se. To begin solidification, the electric heaters are shut off while, at the same time, the water-cooling system is turned on. The experiment was carried out for quaternary aluminum alloy with a superheats of 8% above the liquidus temperature (T_L = 614 °C). Temperature profiles were determined by monitoring through a bank of type k thermocouples positioned along the casting at 5, 10, 15, 20, 35, 45, 60, 85 mm from mold bottom. Temperature readings were collected by data acquisition system (data-logger hardware) at 0.001 s intervals, in order to make for an accurate determination of the thermal parameters. The readings were automatically stored on a personal computer.

After the experiment, cylindrical ingot was sectioned along its vertical axis, mechanically polished with abrasive paper, and subsequently etched with an acid solution (25 ml H_2O, 2.5 ml HF, 25 ml HNO_3, 60 ml HCl) in order to reveal its macrostructure. After the macrostructural analysis, selected transverse sections of the directionally solidified specimens at 5, 10, 15, 20, 35, 45, 60, 85 mm from the mold bottom were polished and etched with a solution 0.5% HF for micrograph examination. It is worth mentioning that thermocouples maintained their positions even after the experiment.

From temperature data collected during experiment, was possible to determine the thermal parameters, such as solidification speed (S_S) and cooling rate ($\dot{T}$). The cooling curves obtained during experiment, were used to provide a function of corresponding time of the liquidus temperature (T_L) passing by each thermocouple located at specific positions from the bottom mold, P = f(t). The derivative of this function with respect to time gave the solidification speed as a function of time and then, from experimental functions (P = f(t) and S_S = f(t)), it was possible to determine an equation for solidification speed as a function of position (S_S = f(P)). The cooling rates ($\dot{T}$) have been determined considering the temperature (T) versus time (t) data immediately after the passage of T_L for the different thermocouples positions. So, cooling rate is determined, for each position of the thermocouples, as $\dot{T} = DT/dt$, consistent with Paradela et al.[9].

An Olympus Optical Microscope (Olympus Corporation, Japan) was used to produce digital images that were analyzed using the Goitaca (https://sourceforge.net/projects/goitacaeq) image processing software in order to measure tertiary dendritic arm spacings (λ_3). Dendrite spacing usually refers to the distance between primary arms (λ_1) of the dendrite. However, if secondary (λ_2) or tertiary arms (λ_3) are present, the spacing will be determined by that smaller dimension. It is well known that smaller dimensions of dendrite arm spacings become more significant for the mechanical properties of the as-cast materials, Paradela et al.[9]. Figure 2 is a representative micrograph of a transverse section from which dendrite spacing (λ_3) measurements were made. Its spacings were determined by averaging the distance between adjacent side branches. A usual expression for the spacing values of dendrites, as indicated by Paradela et al.[9], is

$$\lambda_3 = L/(n-1) \quad (1)$$

where L is the total spacing from the first to the last tertiary arm, and n represents the number of the existing well-developed and parallel dendrite arms in this measuring length L. The average dendritic arm spacing was determined from about 40 to 45 measurements for each examined position along the entire die-casting.

To determine resistance to deformation of quaternary aluminum alloy, microhardness test was carried out at room temperature using Leitz Wetzlar Microhardness Tester. Microhardness tests were measured at least in 20 different regions on the transverse section, using a Vickers pyramidal indenter with a load and loading time of 100 g and 15 s, respectively.

In order to characterize the pores, all samples were cut in the transverse directional plane, from the bottom part of the mold to the top, mounted in conducting Bakelite, and polished to a 0.05 mm finish. Microcomputed tomography also called Micro-CT is a 3D imaging technique, which was performed in present work, using a Phoenix Vtomex GE equipment. Phoenix Vtomex m GE microtomograph is equipped with two X-ray tubes and operated at 100 kV. X-rays were transmitted through the as-cast samples, with a 360º rotation at a step of 0.24º and recorded by the X-ray detector as a 2D projection image. The detection system consists of a Flat-Panel DXR type sensor and reconstruction was performed using Datos/x 2 Reconstruction software, version 2.5.0. The series of X-ray projection images was then computed into cross-sectional images through the computational process called "reconstruction". These slices can be analyzed, further processed into 3D images. These said slices, which constitute the interest volume, were joined using the FDK (Feldkamp-Davis-Kress) algorithm to generate the 3D image, Figure 3.

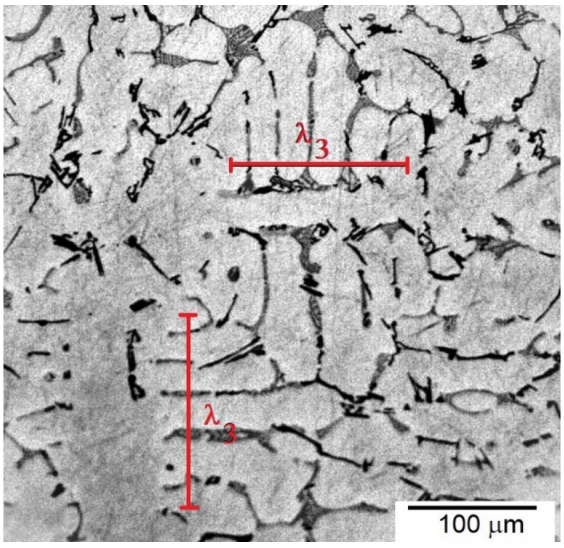

Figure 2. Transverse micrograph of quaternary Al – 5 wt.% Si – 4 wt.% Cu – 1 wt.% Ni alloy, which illustrates measuring the tertiary dendrite-arm spacings (λ_3).

3. Results and Discussion

Figure 4 shows the phase diagram of the quaternary Al – 5 wt.% Si – 4 wt.% Cu – 1 wt.% Ni alloy calculated by Thermo-Calc software using the aluminum-based alloys databases - TCAL9[10]. For quaternary aluminum alloy, in cooling process the solidification begins at liquidus temperature of 614 ºC and ends when the temperature reaches its solidus temperature of 522 ºC, as indicated in Figure 4, highlighting the liquid−solid transformation region. It is worth mentioning that solidification interval is determined by the difference of liquidus and solidus temperatures ($\Delta T_S = T_L - T_S$) and as-cast alloys with wide solidification interval make them susceptible to segregation during the solidification process.

Figure 5 shows Thermo-Calc Scheil simulation for the quaternary aluminum alloy.

Through the graph of temperature versus solid fraction, one can predict the growth sequence of each solid phase during cooling process. At the 614 ºC, the FCC_Al solid phase starts to grow as a primary solid, and at 522 ºC all the solutes-enriched liquid will give rise to a 2% eutectic fraction. Calculations by Scheil model, revealed precipitation of solid phases during cooling. Between 614 and 560 ºC, one can see liquid and solid (LIQUID + FCC_A1) and, from 560 to 552 ºC were observed

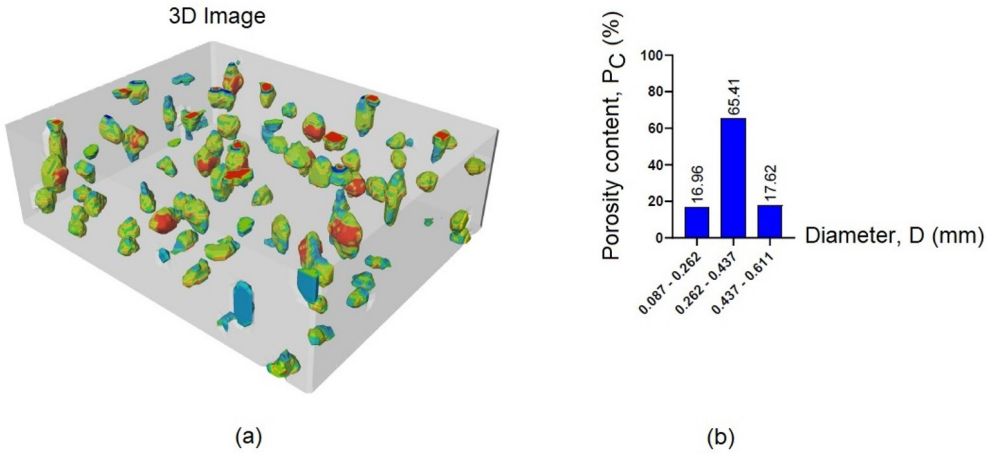

Figure 3. Porosity as observed for as-cast sample taken at position of 85 mm: a) 3D Image; and b) Porosity content versus diameter.

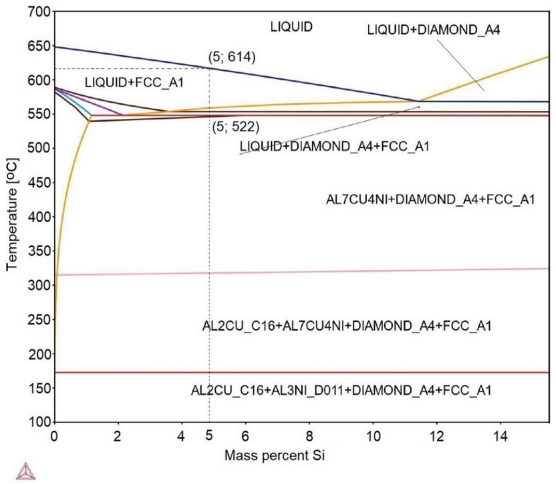

Figure 4. Phase diagram of Al – 5 wt.% Si – 4 wt.% Cu – 1 wt.% Ni Ag alloy calculated by Thermo-Calc software using the aluminum-based alloys databases - TCAL9, Ref[10].

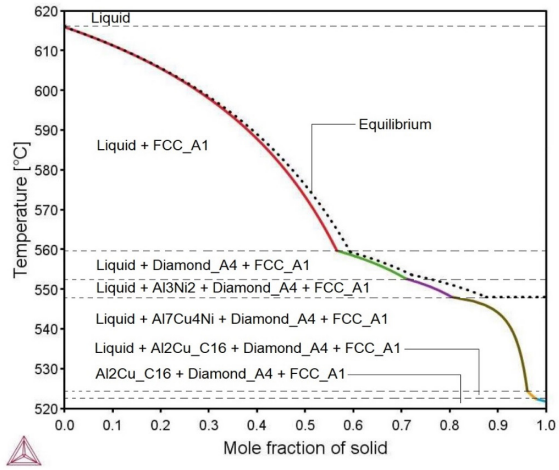

Figure 5. Equilibrium Scheil model revealing precipitation of solid phases during cooling process.

liquid and two solids (LIQUID + DIAMOND_A4 + FCC_A1). From 552 to 546 °C, were found liquid and three solids (LIQUID + Al_3Ni_2 + DIAMOND_A4 + FCC_A1), while between 546 and 525 °C were observed liquid and also three solids which are LIQUID + Al_7Cu_4Ni + DIAMOND_A4 + FCC_A1. Finally, between 525 and 522 °C, we can see liquid and three solid (LIQUID + Al_2Cu_C16 + DIAMOND_A4 + FCC_A1).

Figure 6 shows corresponding experimental validation of liquidus and solidus temperature for quaternary aluminum alloy. In addition to the cooling curve, its first and second derivative are plotted in this same graph.

It is worth mentioning that the cooling curve is obtained from slow solidification conditions, i.e., without any water-cooled solidification system. The slow solidification experiment was performed with a cooling rate at around 0.09 °C/s. It is interesting to observe that the cooling rate was calculated from the slope of the cooling curve in the liquid region,

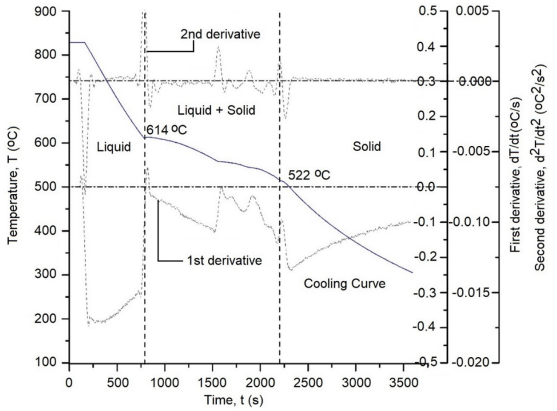

Figure 6. Slow cooling curve and its first and second derivatives with corresponding phase transformations.

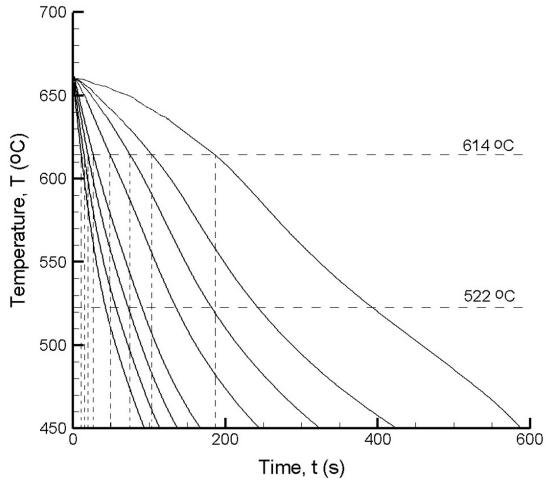

Figure 7. Temperature (T) versus time (t).

Refs[12,13]. Figure 6 demonstrates that solidification process begins at about 614 °C, as indicated by the change in the cooling curve caused by the release of latent heat. The cooling curve was plotted, and the first and second derivatives of the cooling curves were produced using the Tecplot 360 software to analyze the data. After solidification completion at 522 °C, the slope of cooling curve is again altered. These slope changes in cooling curve provoke an abrupt increase in second derivative values, indicating the beginning and end of solidification experiment. Between liquid and solidus temperatures, one can see peaks of the second derivative values, these abrupt increase in their values, are due to the subsequent transformations in the solid phase. In this work, approach based on the second derivative curve was adopted to determine the beginning and end of solidification process and subsequent phase transformation.

A file containing the temperature versus time data for upward solidification experiment under transient conditions of heat extraction is presented in Figure 7. This graph shows the cooling curves obtained by means of the eight thermocouples placed at positions from the 5 to 85 mm along the casting height. The pouring temperature was set at around 660 °C,

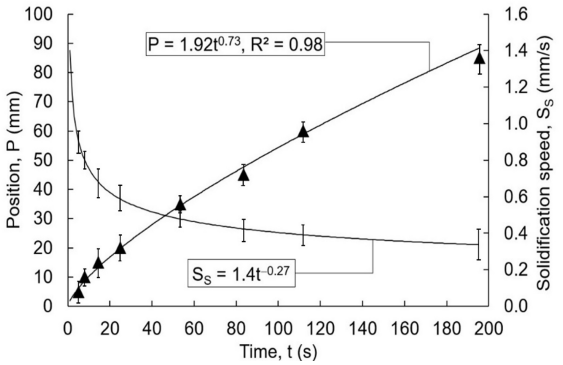

Figure 8. Position (P) and solidification speed (S_S) as a function of time (t).

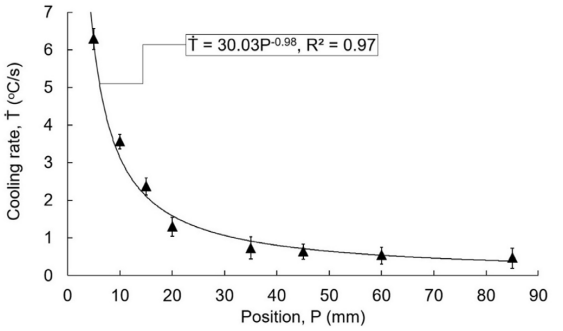

Figure 9. Cooling rate (Ṫ) versus position (P).

according to the Paradela et al.[9]. Figure 7 exhibit the cooling profiles for each positions from 5 to 85 mm and values of the passing time of liquidus temperature.

Through the cooling profiles in Figure 7, the position of the liquidus temperature (T_L = 614 °C) was determined as a function of time by regression from experimental data, as depicted in Figure 8. From this function (P=f(t)), the value of solidification speed (S_S=f(t)) were calculated as a function of the time by computing the time derivative. Figure 8 also displays these results.

Using P = f(t) and S_S = f(t) and rearranging the terms, it was possible to determine an equation for solidification speed as a function of position (S_S = f (P)), $S_S = 2.28P^{-0.45}$. Cooling rate (Ṫ = f (P)) for different positions along the casting is shown in Figure 9. It can be observed that cooling rate (Ṫ) decreases with position (P), which is evidenced by experimental equation $\dot{T} = 30.03P^{-0.98}$.

This profile is because the water-cooling system favors higher cooling rates in the regions close to the mold bottom, which decreases along the length of the casting due to an increase in thermal resistance of the new solidified layers. The cooling rate has been determined considering the temperature versus time data immediately after the passage of the liquidus temperature in each position of the casting. It is worth mentioning that temperature data were collected at intervals of 0.001 s, in order to determine the cooling rates accurately. This thermal parameter, cooling rate, related to the position of castings, is an aspect acting during the solidification experiment, which affects the changes in the size and morphology of the as-cast microstructure.

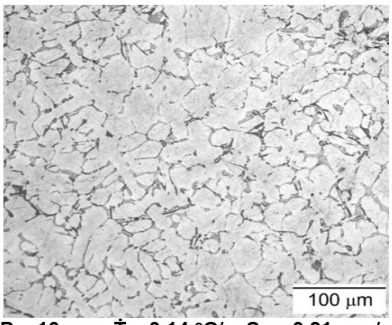

P = 10 mm, Ṫ = 3.14 °C/s, S_S = 0.81 mm/s; and λ_3 = 24.3 µm ± 4.1

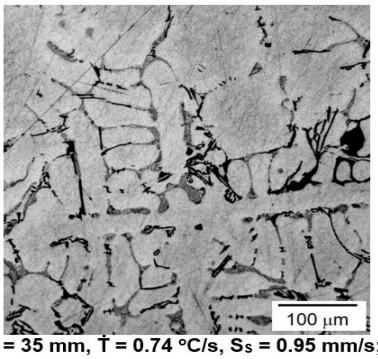

P = 35 mm, Ṫ = 0.74 °C/s, S_S = 0.95 mm/s; and λ_3 = 32.7 µm ± 3.4

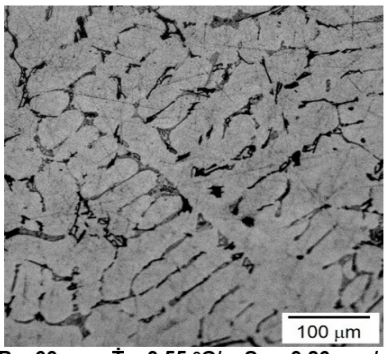

P = 60 mm, Ṫ = 0.55 °C/s, S_S = 0.86 mm/s; and λ_3 = 42.4 µm ± 3.0

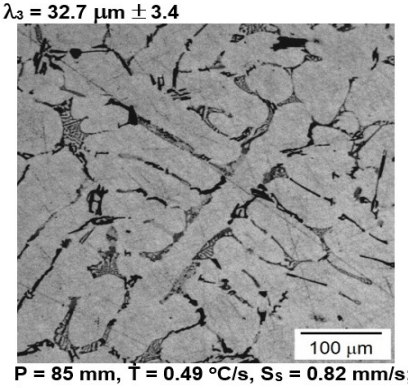

P = 85 mm, Ṫ = 0.49 °C/s, S_S = 0.82 mm/s; and λ_3 = 48.3 µm ± 3.5

Figure 10. Photomicrographs of as-cast samples taken from transverse sections.

Figure 10 shows the microstructures from transverse samples taken along the casting.

Below each photomicrographs, one can see information on sample position (P) in the casting, thermal parameters ($\dot{T}$ and S_S), and tertiary dendrite arm spacing (λ_3). One can see in Figure 10, that from very fine to large dendrites, the changes found in the size of the microstructure are due to a wide range of thermal parameters observed during the upward unidirectional solidification. The solidification apparatus with water-cooled system is very useful when high cooling rates and solidification speed are intended to be achieved. According to Ferreira et al.[14], the thermal parameters such as cooling rate and solidification speed exerts a strong influence on the mechanical properties and quality of the final product, as the microstructure of the material is refined when solidification proceeds at a high cooling rate. The pictures shown in Figure 10 show how dendritic arm spacings and the size of dendrites are refined as the distance to the mold bottom is reduced. At room temperature, the as-cast microstructure consists of primary dendrites (Al-rich, FCC_A1) surrounded by a finely divided eutectic mixture of four solid phases (Al_2Cu_C16 + Al_3Ni_D011 + DIAMOND_A4 + FCC_A1), Figure 11. The dendrite (FCC_A1) is represented by a surface with a whitish appearance, while the eutectic mixture is represented by a stained surface with a darkened appearance.

Tertiary dendritic arm spacings versus thermal parameters ($\dot{T}$ and S_S) are shown in Figure 12. It can be observed in Figure 12 that the tertiary dendritic arm spacing decreases with thermal parameters, which is evidenced by experimental equations ($\lambda_3 = 33.69\dot{T}^{-0.28}$ and $\lambda_3 = 32.68S_S^{-1.25}$). The profiles depicted in Figure 12 correspond to experimental equations obtained from experimental data for quaternary aluminum alloy considered in our solidification experiment. The profiles are in agreement with the published literature, Meza et al.[15], and show the effects of thermal parameters on the microstructural patterns. This effect translates to the as-cast microstructure growth, i.e., higher values of thermal parameters near the mold bottom favor a more refined microstructure, whereas lower values of these thermal parameters close to the top of the casting contribute effectively to yield a coarser microstructure. Higher thermal parameters with a short solidification time can induce the finely dispersed intermetallic phases and most refined microstructure, as consequence, the mechanical properties, such as microhardness, are correspondly increased.

Transverse as-cast samples were cut from eight positions close to each thermocouple, with the purpose of determining a relationship between cooling rate ($\dot{T}$), tertiary dendritic arm spacing (λ_3) and Vickers microhardness (H_V), as shown in Figure 13. The H_V versus $\dot{T}$ are shown in Figure 13a, where a variation of this mechanical property with $\dot{T}$ can be

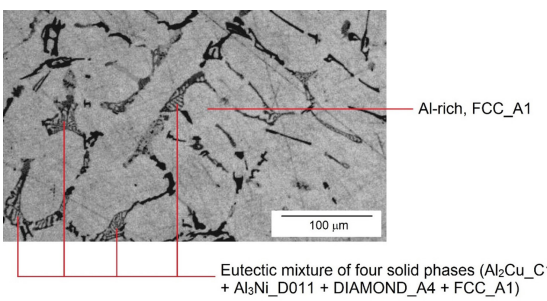

Figure 11. Primary dendrite surrounded by a eutectic mixture.

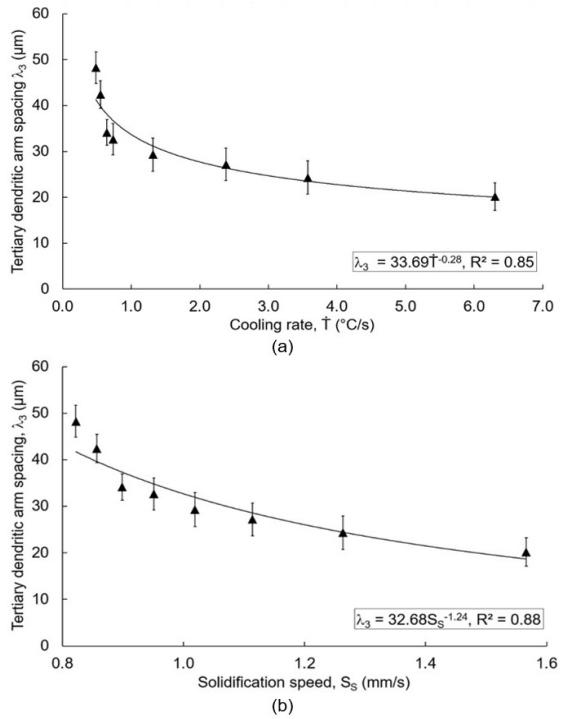

Figure 12. Tertiary dendritic arm spacing (λ_3) versus: a) Cooling rate ($\dot{T}$); and b) Solidification speed (S_S).

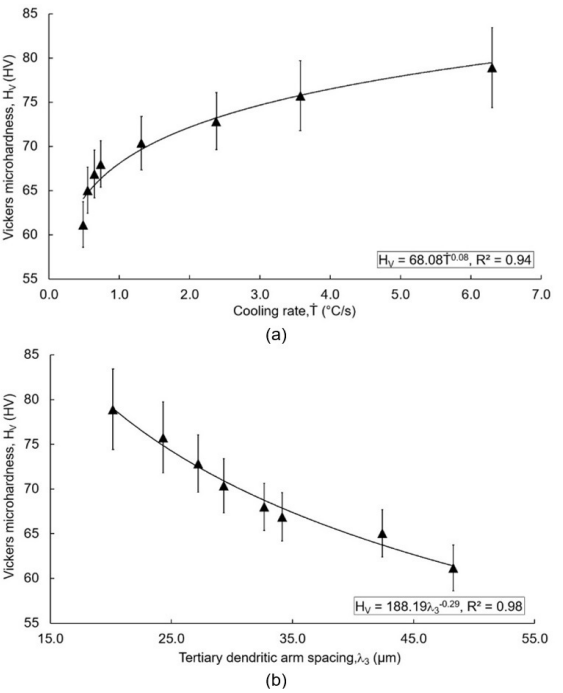

Figure 13. Vickers microhardness versus: a) Cooling rate ($\dot{T}$); and b) Tertiary dendritic arm spacing (λ_3).

observed. As expected, in positions near the water-cooled system, where higher cooling rates are found, an improvement in microhardness is observed. In contrast, one can see an inverse trend in the Figure 13b, the microhardness starts a gradual decrease with tertiary dendritic arm spacing. The cooling rate and tertiary dendritic arm spacing are key factors acting interactively during the solidification experiment, which servers to condition the changes in the microhardness, affecting strongly the quality of the final product. Higher cooling rates and solidification speeds favors a shorter local solidification time, resulting in decreased dendritic arm spacing and increased microhardness. This happens due to as-cast microstructure refinement reduces grain size during the solidification experiment. This grain refinement strengthening mechanism increases microhardness by improving the its strength and reducing the likelihood of cracks forming. It is known in the literature that higher cooling rate has a strong influence on the increasing the nucleation rate and growth kinetics of solid phase, Ferreira et al.[14]. For higher nucleation rates during solidification experiment, result in higher number density of primary solid (Al-rich, FCC_A1) formed during solidification. This in turn, favors a reduction in tertiary dendritic spacings (λ_3), resulting in a more refined microstructure. With the increase in the cooling rate and solidification speed, tertiary dendritic arm spacing was greatly reduced. According to the Ferreira et al.[14], relatively high cooling rates significantly increase microsegregation in primary solid (Al-rich, FCC_A1) due to the transition of solidification from near-equilibrium to the non-equilibrium conditions. During the solidification process under high cooling rates conditions, the increase in microsegregation level in primary solid and refinement of dendrites, lead to improved microhardness in the as-cast alloy.

Upward solidification apparatus also was used to investigate the effects of cooling rate and dendrite arm spacings on the porosity formation in as-cast samples of the quaternary aluminum alloy. Figure 14 presents the evolution of 3D porosity, obtained using the Phoenix Vtomex m GE microtomograph, for samples taken along the casting. One can see to the right side of this figure, information concerning the cooling rate ($\dot{T}$), tertiary dendritic arm spacing (λ_3), as well as position (P) of each sample along the casting. By considering the 3D porosity evolution presented in Figure 14, we can see an increase in the porosity content values with increasing distance from the water-cooled bottom, these results are consistent with those found by Dantas et al.[16] and Cao et al.[17]. However, experimental results of porosity evolution with cooling rate and tertiary dendritic arm spacing present an inverse behavior, i.e., porosity content values decrease with increasing $\dot{T}$ and λ_3. By considering the 3D image presented in Figure 14, one can see a slight increase in the porosity size along the casting. This porosity dependence with the position along the casting, can be related to the fact that upward unidirectional solidification technique allows wide values ranges of cooling rates and dendritic arm spacings, Okayasu et al.[18].

The distribution of pore sizes along the casting is shown in Figure 15. One of the most severe types of defects found in castings, is porosity, and aluminum alloys are known for their susceptibility to porosity formation during solidification.

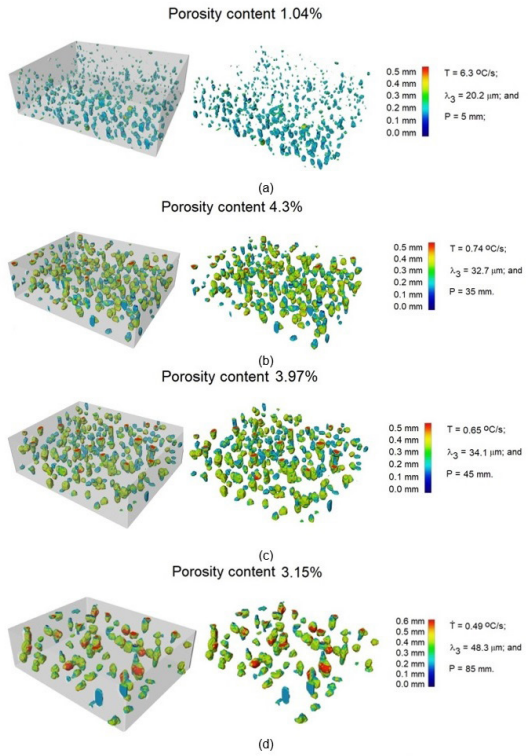

Figure 14. Porosity evolution along the casting.

These porosities manifest themselves in different ways during casting. They form in the mushy zone, and their morphologies and size are distinct, Bhagavath et al.[19]. Porosity is among the most common casting defects, occurs when a pocket forms due to air or gas trapped in the metal during solidification, this is known as gas porosity. Porosity is also caused by the metal shrinking, leaving contraction voids in the metal during the casting, this is called micro shrinkage. Morphology of gas porosity, resemble a spherical shape with smaller sizes. On the other hand, morphology of contraction voids (micro shrinkage) is always irregular with higher sizes and elongated, Bhagavath et al.[19]. Up to the position of 10 mm, one can see that gas porosity with smaller sizes, between 0.087 - 0.262 mm, were predominant in casting. From 0 to 10 mm position, pore percentage for the mentioned size range (0.087 - 0.262 mm), is to 100, 98.47 and 69.52% of pore size distribution found during solidification experiment, Figure 15a-c. Results obtained from pores size distribution, have pointed out that the gas porosity is main causes of pore formation up to position of 10 mm. However, from the 20 to 85 mm position, it can be observed that higher sizes pores have become predominant in the casting. These experimental data depicted in Figure 15d-i, point out that the porosity formation from 20 mm position, is mainly due to the lower cooling rates, favoring porosity formation with higher sizes. At lower cooling rates, the hydrogen segregation rate from solid phase is slow, and the relatively slow growth rate of porosity is favored, but once the porosities are nucleated, they have enough time to absorb hydrogen for growth. The rate of hydrogen absorption by gas porosity is higher than that hydrogen segregation from

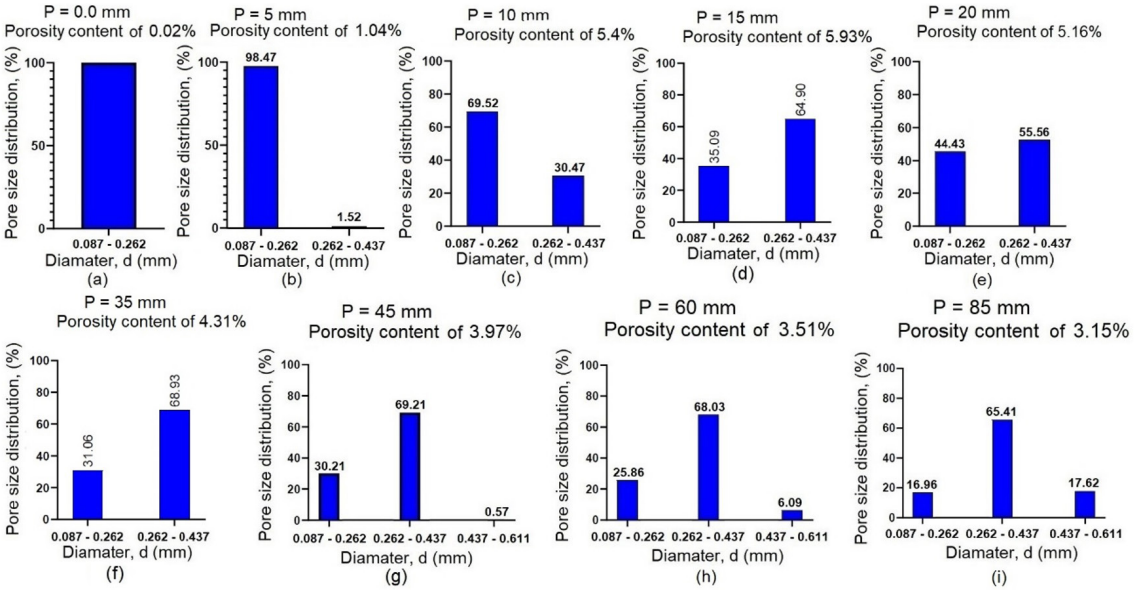

Figure 15. Distribution of pore sizes for different positions along the casting.

solid phase, so it is difficult for new porosity nucleation. In this case, the porosity inside the alloy, have the larger sizes, Okayasu et al.[18].

The relationships between position (P), cooling rate ($\dot{T}$), tertiary dendritic arm spacing (λ_3) and porosity content (P_C) are depicted in Figure 16.

By considering the results presented in Figure 16a-c, we can to conclude that both dendritic arm spacing and cooling rate are important factors affecting the porosity formation during solidification experiment. The increase in the cooling rate leads to a decrease in the content and size porosity. Higher cooling rates favors reduction of porosity growth time, thus limiting its size and content. Porosity with lower sizes, were observed from water-cooled bottom to 10 mm position. We can see an abrupt increase in the gas porosity values with increasing distance from water-cooled bottom, which is due to lower cooling rates during solidification experiment. As the quaternary alloy solidifies, the solubility of hydrogen in the liquid is strongly affected by the cooling rate imposed during experiment, which conditions the formation and growth of pores, Mahomed and Kleynhans[20]. It is worth mentioning that with first derivative test of the experimental equation presented in Figure 16b, we can find maxima porosity content value of 5.9% for a cooling rate equal to 2.88 °C/s. It is interesting to note that P_c = 5.9% and $\dot{T}$ = 2.88 °C/s, represents a maxima point of the experimental equation, i.e. both to the left of this point and to its right the experimental equation has a decreasing profile. The highest cooling rate values were observed in regions very close to the water-cooled system. According to the Dantas et al.[16], water-cooled system is usually used to optimize the cooling rates, and have several advantages as decrease of local solidification time, finer grain structure and decrease of cellular spacing. These factor, in turn, avoid porosity formation during solidification process, so porosity content can be minimized.

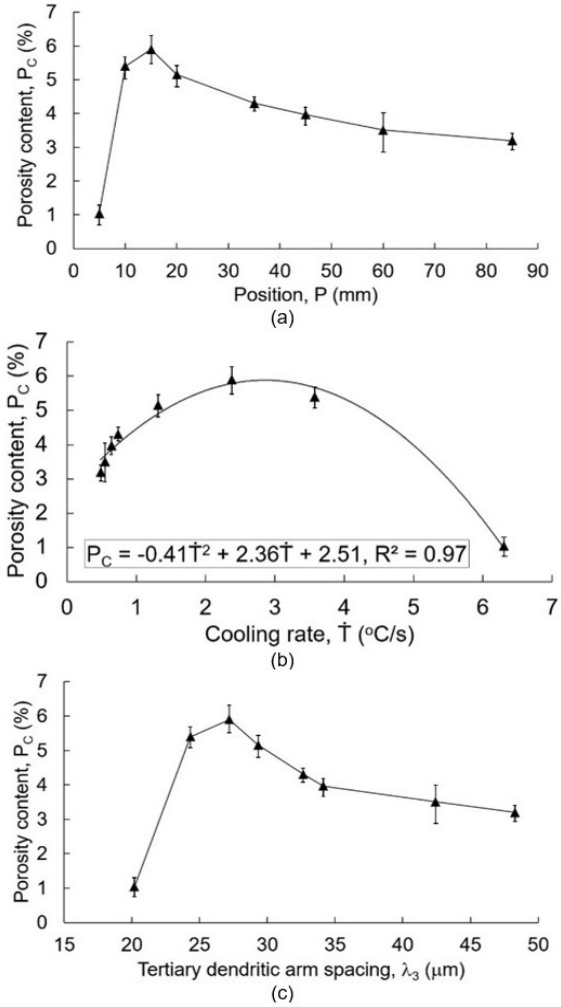

Figure 16. Porosity content versus: a) Position (P); b) Cooling rate ($\dot{T}$); and c) Tertiary dendritic arm spacing (λ_3).c

4. Conclusions

This work investigated the phase formation, as-cast microstructure, 3D porosity and microhardness for a quaternary 5 wt.% Si – 4 wt.% Cu – 1 wt.% Ni alloy obtained under transient heat-flow conditions. The conclusions are presented below.

1. The sequence of phase formation was calculated according to the Thermo-Calc Scheil simulation. The Scheil model predicted that the formation of the FCC_Al solid phase starts to grow as a primary solid at 614 °C, corresponding to the liquidus temperature, and the solidus, temperature was 522 °C when all the solutes-enriched liquid will give rise to a 2% eutectic fraction;
2. Corresponding experimental validation of phase formation sequence with liquidus and solidus temperature, it was obtained with slow cooling curve and its first and second derivatives;
3. Both thermal parameters decrease faster in the positions near the water-cooled system and these parameters become almost constant as move away from the mold bottom. This behavior is due to an increase in the thermal resistance of the newly solidified layers, which hampers heat extraction during solidification experiment;
4. Due to the cooling rates imposed during the directional solidification and composition of quaternary aluminum alloy, a dendritic microstructure was predominant along casting;
5. Experimental equations associating tertiary dendrite arm spacing with the thermal parameters were determined, showing that the increase in cooling rate has induced a decrease in the dendrite arm spacing;
6. Higher cooling rates and refined microstructures were key factors acting during the solidification, which served to conditions the changes in the Vickers microhardness along the casting;
7. Upward solidification apparatus was used to investigate the influence of cooling rate and dendritic arm spacing on the porosity formation along the casting. By considering the 3D image of pores formation, we can see a slight increase in the porosity size along the casting. This effect of position on the porosity size, can be related to the fact that upward directional solidification allows wide values ranges of thermal parameters and dendrite arm spacings;
8. Through the 3D image analysis, it can be investigated distribution of pores sizes along the casting. Up to the position of 10 mm, one can observe that gas porosity with smaller sizes, were predominant in casting. From mold bottom to position of 10 mm, results obtained for pores size distribution, have pointed out that the gas porosity was main causes of pore formation in casting;
9. From 20 mm position, it can be observed that higher sizes pores have become predominant in the casting; and
10. By considering the results presented, we can to conclude that both dendritic arm spacing and cooling rate are important factors affecting the porosity formation during solidification experiment. The increase in the cooling rate and decrease in the dendrite arm spacing, leads to a decrease in the content and size of the porosity. Higher cooling rates favors reduction of pores growth time, thus limiting its size and content.

5. Acknowledgments

The authors are grateful to National Council for Scientific and Technological

Development (CNPq, nº 302847/2022-7, PQ - 2022) for financial support.

6. References

1. Farina ME, Bell P, Ferreira CRF, Dedavid BA. Effects of solidification rate in the microstructure of Al-Si5Cu3 aluminum cast alloy. Mater Res. 2017;20(Suppl. 2):273-8. http://doi.org/10.1590/1980-5373-mr-2017-0083.
2. Li JH, Ludwig TH, Oberdorfer B, Schumacher P. Solidification behaviour of Al–Si based alloys with controlled additions of Eu and P. Int J Cast Met Res. 2018;31(6):319-31. http://doi.org/10.1080/13640461.2018.1480891.
3. Canales A, Talamantes-Silva J, Gloria D, Valtierra S, Colás R. Thermal analysis during solidification of cast Al-Si alloys. Thermochim Acta. 2010;510(1-2):82-7. http://doi.org/10.1016/j.tca.2010.06.026.
4. Farahany S, Ourdjini A. Effect of cooling rate and silicon refiner/modifier on solidification pathways of Al-11.3Si-2Cu-0.4Fe alloy. Mater Manuf Process. 2013;28:657-663. http://doi.org/10.1080/10426914.2013.763972.
5. Farahany S, Ourdjini A, Idris MH, Shabestari SG. Computer-aided cooling curve thermal analysis of near eutectic Al–Si–Cu–Fe alloy. J Therm Anal Calorim. 2013;114(2):705-17. http://doi.org/10.1007/s10973-013-3005-7.
6. Cruz CB, Kakitani R, Xavier MGC, Silva BL, Garcia A, Cheung N, et al. Transient unidirectional solidification, microstructure and intermetallics in Sn-Ni alloys. Mater Res. 2018;21(Suppl. 1):1-11. http://doi.org/10.1590/1980-5373-mr-2017-1099.
7. Silva CCS, Santos VT, Lobo FG, Silva MR, Santos GA, Vasconcellos SP, et al. Phase stability and unidirectional solidification in a Ni-Al bronze. J Mater Res Technol. 2023;25:2240-50. http://doi.org/10.1016/j.jmrt.2023.06.030.
8. Tamura T, Li M, Takahashi K, Inoue E. Improved solidification structures and mechanical properties of Al–20 wt% Sn alloys processed by an electromagnetic vibration technique. Mater Sci Eng A. 2023;862:144416. http://doi.org/10.1016/j.msea.2022.144416.
9. Paradela KG, Baptista LAS, Sales RC, Felipe P Jr, Ferreira AF. Investigation of thermal parameters effects on the microstructure, microhardness and microsegregation of Cu-Sn alloy directionally solidified under transient heat flow conditions. Mater Res. 2019;22(4):e20190259. http://doi.org/10.1590/1980-5373-mr-2019-0259.
<soft>10. Thermo-Calc Software. Thermo-Calc Software AB. Solna: Thermo-Calc Software; 2025.
11. Ahmad R, Asmael MBA. Influence of cerium on microstructure and solidification of eutectic Al-Si piston alloy. Mater Manuf Process. 2016;31(15):1948-57. http://doi.org/10.1080/10426914.2015.1127942.
12. Ahmad R, Asmael MBA. Influence of lanthanum on solidification, microstructure, and mechanical properties of eutectic Al-Si piston alloy. J Mater Eng Perform. 2016;25(7):2799-813. http://doi.org/10.1007/s11665-016-2139-8.
13. Ahmad R, Sheggaf ZM, Asmael MBA. Effect of praseodymium and erbium additions on solidification characteristics, microstructure and mechanical properties of as–cast ZRE1 magnesium alloy. Materialwiss Werkstofftech. 2017;48(3-4):218-25. http://doi.org/10.1002/mawe.201600766.

14. Ferreira AF, Moura LJ, Dantas BS, Brum FJB, Garção WJL, Sales RC. Investigations on metallurgical parameters in hypoeutectic Al–Si alloys under upward directional solidifications. Int J Adv Manuf Technol. 2022;121(11-12):7359-82. http://doi.org/10.1007/s00170-022-09836-3.
15. Meza ES, Bertelli F, Goulart PR, Cheung N, Garcia A. The Effect of the growth rate on microsegregation: experimental investigation in hypoeutectic Al–Fe and Al–Cu alloys directionally solidified. J Alloys Compd. 2013;561:193-200. http://doi.org/10.1016/j.jallcom.2013.01.180.
16. Dantas BS, Garção WJL, Peixoto FM, Guimarães NA, Tomaszewski IMS, Ferreira AF. Microstructural patterns, microsegregation, porosity, and mechanical properties of hypoeutectic Al-Fe alloy, and its dependency with solidification thermal parameters. Mater Res. 2022;25:e20220187. http://doi.org/10.1590/1980-5373-mr-2022-0187.
17. Cao F, Li H, Ning Z, Jia Y, Gu X, Yu L, et al. The formation mechanism of porosity for spray-deposited 7075 alloy. Mater Res. 2015;18(Suppl. 1):89-94. http://doi.org/10.1590/1516-1439.328414.
18. Okayasu M, Ohkura Y, Takeuchi S, Takasu S, Ohfuji H, Shiraishi T. A study of the mechanical properties of an Al–Si–Cu alloy (ADC12) produced by various casting processes. Mater Sci Eng A. 2012;543:185-92. http://doi.org/10.1016/j.msea.2012.02.073.
19. Bhagavath S, Cai B, Atwood R, Li M, Ghaffari B, Lee PD, et al. Combined deformation and solidification-driven porosity formation in aluminum alloys. Metall Mater Trans, A Phys Metall Mater Sci. 2019;50(10):4891-9. http://doi.org/10.1007/s11661-019-05378-8.
20. Mahomed N, Kleynhans HA. Reducing shrinkage porosity in high-performance steel castings: case of an ASME B16.34 gate valve body: part 2—simulation and experimental verification. Int J Met Cast. 2019;13(2):463-72. http://doi.org/10.1007/s40962-018-0275-7.

Data Availability

The dataset supporting the results of this work is not publicly available.